

A Metastable Pentagonal 2D Material Synthesized by Symmetry-Driven Epitaxy

Lina Liu^{1,4,7, #}, Yujin Ji^{2, #}, Marco Bianchi³, Saban M. Hus⁵, Zheshen Li⁶, Richard Balog⁷, Jill A. Miwa³, Philip Hofmann³, An-ping Li⁵, Dmitry Y. Zemlyanov^{4, *}, Youyong Li^{2, *}, Yong P. Chen^{1,4,7,8*}

¹Department of Physics and Astronomy, Purdue University, West Lafayette, Indiana, 47907, USA

²Institute of Functional Nano and Soft Materials, Soochow University, Suzhou, Jiangsu Province, 215123, China

³Department of Physics and Astronomy and Villum Center for Dirac Materials, Aarhus University, 8000, Aarhus C, Denmark

⁴Birck Nanotechnology Center, Purdue University, West Lafayette, Indiana, 47907, USA

⁵Center for Nanophase Materials Sciences, Oak Ridge National Laboratory, Oak Ridge, TN, 37831, USA

⁶Department of Physics and Astronomy and center for Storage Ring Facilities (ISA), Aarhus University, 8000, Aarhus C, Denmark

⁷Department of Physics and Astronomy and Villum Center for Hybrid Quantum Materials and Devices, Aarhus University, 8000, Aarhus C, Denmark

⁸Purdue Quantum Science and Engineering Institute and School of Electrical and Computer Engineering, Purdue University, West Lafayette, Indiana, 47907, USA

Corresponding to: yongchen@purdue.edu

yyli@suda.edu.cn

dzemlian@purdue.edu

Abstract

Most two-dimensional (2D) materials experimentally studied so far have hexagons as their building blocks. Only a few exceptions, such as PdSe₂, are lower in energy in pentagonal phases and exhibit pentagons as building blocks. While theory has predicted a large number of pentagonal 2D materials, many of them are metastable and their experimental realization is difficult. Here we report the successful synthesis of a metastable pentagonal 2D material, the monolayer pentagonal PdTe₂, by symmetry-driven epitaxy. Scanning tunneling microscopy and complementary spectroscopy measurements are used to characterize the monolayer pentagonal PdTe₂, which demonstrates well-ordered low-symmetry atomic arrangements and is stabilized by lattice matching with the underlying Pd(100) substrate. Theoretical calculations, along with angle-resolved photoemission spectroscopy, reveal monolayer pentagonal PdTe₂ is a semiconductor with an indirect bandgap of 1.05 eV. Our work opens an avenue for the synthesis of pentagon-based 2D materials and gives opportunities to explore their applications such as multifunctional nanoelectronics.

Since the first few pentagonal 2D materials, pentagonal graphene¹ and noble metal dichalcogenides², were predicted several years ago, research interest has been growing in this subgroup of 2D materials due to their unique properties and potential applications in nanoelectronics, optoelectronics and thermoelectrics^{3,4}. Unlike the much more studied hexagon-based 2D materials, the building blocks for pentagonal 2D materials are pentagons. Due to the well-known pentagonal tiling rule, where regular pentagons cannot tile a plane, pentagonal 2D materials tend to form puckered layers. Such a puckered pentagon-based structure presents low crystallographic symmetry, leading to an orthorhombic crystal structure with rectangular unit cells⁵. The low crystallographic symmetry introduces large in-plane anisotropy and low thermal conductivity, making them promising candidate materials for future anisotropic electronics and thermoelectrics⁶⁻¹⁰. The puckered layers in pentagonal 2D materials also induce renormalization of bond lengths and angles, resulting in decreased layer thickness and increased layer flexibility¹¹. This makes pentagonal transition metal dichalcogenides (TMDCs) monolayers ~40-50% thinner compared to hexagonal TMDC monolayers¹¹ and could facilitate applications in flexible devices and wearable electronics. Furthermore, many other fascinating properties have been predicted for pentagonal 2D materials such as ultrahigh strength of pentagonal graphene¹, room temperature quantum spin Hall effect of pentagonal SnX₂ (X=S, Se, Te)¹², magnetic Dirac fermions of pentagonal MoS₂¹³ and ferromagnetism of semiconducting pentagonal VTe₂¹⁴, indicating that the pentagonal 2D materials are not only promising materials for novel applications but also demonstrate great potentials in fundamental studies of new quantum states and phenomena.

Although pentagonal 2D materials have been theoretically predicted for years, few of them have been experimentally studied so far³. Only recently, PdSe₂ together with analogous PdPSe and PdPS, a few materials with pentagonal structures as thermodynamically stable phases, start to be investigated¹⁵⁻¹⁸ (note their bulk crystals, with the orthorhombic structure, were studied much earlier^{19,20}). Their properties including high mobility and large in-plane anisotropy have been unveiled, which facilitates their applications in functional nanoelectronics¹⁵⁻¹⁸. In addition, giant non-linear optical activity has been observed in PdSe₂^{21,22}, implying its potential in optoelectronics. More interestingly, the pentagonal structure offers PdSe₂ great flexibilities for structural reconstruction, which provides opportunities for phase engineering²³ and enables interlayer manipulation²⁴. However, in contrast to PdSe₂,

many pentagon-based 2D materials are metastable²⁵ (Supplementary Fig. 1), which makes the direct synthesis of these materials more challenging. Although previously some metastable phases of hexagon-based 2D TMDCs (such as 1T and 1T' phases of MoS₂) have been synthesized²⁶⁻²⁸, the direct synthesis of pentagon-based metastable phases has never been demonstrated. The lack of proper ways to synthesize and stabilize pentagonal 2D materials (particularly the metastable ones) has largely hindered the exploration of this unique class of 2D materials.

Here, we report the direct synthesis of metastable monolayer pentagonal PdTe₂. So far, all synthesized PdTe₂ (both bulk and 2D layers) demonstrate hexagonal 1T structures²⁹⁻³¹ since its hexagonal phase is energetically favorable with the lowest formation energy³². Based on our density functional theory (DFT) calculations, the formation energy for monolayer pentagonal PdTe₂ is only 0.04 eV/atom higher than that of the monolayer hexagonal PdTe₂ (Supplementary Fig. 1), suggesting potential feasibility to synthesize the pentagonal phase. Here, we use epitaxial growth, which is an efficient way to grow high-quality 2D materials^{33,34}, for the synthesis of pentagonal PdTe₂. During epitaxy, the substrate symmetry plays a crucial role and the as-grown structure can be well-controlled and stabilized due to lattice match with the substrate³⁵. We demonstrated the synthesis of monolayer pentagonal PdTe₂ by symmetry-driven epitaxy through direct tellurization of Pd(100) surface, whose lattice exhibits good lattice-match with that of pentagonal PdTe₂. The successful growth of monolayer pentagonal PdTe₂ was confirmed by various structural and spectroscopic characterizations. Comprehensive scanning tunneling microscopy (STM) measurements and simulations, along with low electron energy diffraction (LEED) proved the atomic structures of pentagonal PdTe₂. X-ray photoelectron spectroscopy (XPS) measurements verified the formation of PdTe₂ and the monolayer thickness. Phonon dispersions were revealed by DFT calculations and corresponding lattice vibrational modes were observed in the high-resolution electron energy loss spectroscopy (HREELS) spectra. The DFT calculations revealed that the monolayer pentagonal PdTe₂ is a semiconductor with an indirect bandgap of 1.05 eV, which is consistent with the scanning tunneling spectroscopy (STS) result. Meanwhile, the valence bands of the monolayer pentagonal PdTe₂ were measured by angle-resolved photoemission spectroscopy (ARPES). The direct synthesis, along with the comprehensive measurements of atomic structures, phonon dispersions and electronic

structures of monolayer pentagonal PdTe₂, will greatly accelerate the research field of pentagonal 2D materials.

We selected different facets of Pd single crystals as substrates for the epitaxial growth of different phases of PdTe₂. By taking advantage of the symmetries of the underlying substrates, hexagonal and pentagonal monolayer PdTe₂ were successfully synthesized through direct tellurization of Pd(111) and Pd(100) surfaces, respectively (Fig. 1a). The as-grown hexagonal monolayer PdTe₂ exhibits conventional 1T structure (Fig. 1b and 1c) with $(\sqrt{3}\times\sqrt{3})R30^\circ$ atomic arrangements, which has been thoroughly discussed in our previous work³⁶.

In this work, we focus on the pentagonal phase of PdTe₂ grown on Pd(100). Before growth, the surface of Pd(100) was freshly cleaned by repeated sputtering and annealing in ultrahigh vacuum (UHV). After cleaning, Pd atoms on the surface were full of dangling bonds and chemically reactive. Then Te was deposited on the Pd(100) substrate. Annealing at 500 °C induced the formation of pentagonal PdTe₂, which as shown below exhibits lattice-match with the Pd(100) substrate (details of growth could be found in the Supplementary Fig. 2). This lattice-match serves as the driving force for the growth of the pentagonal phase of PdTe₂. Pentagonal PdTe₂ presents low crystallographic symmetry with monoclinic space group⁸ of $P2_1/c$, which is significantly different from the hexagonal PdTe₂ with high symmetry space group³⁷ of $\bar{P}3m1$. Its out-of-plane geometries are puckered (Fig. 1a) and its projected in-plane atomic arrangements demonstrate pentagons as the building blocks (Fig. 1d). The projected in-plane structure exhibits a rectangular unit cell (Fig. 1d), with a tetra-coordination^{5,15} for Pd atoms (where each Pd atom bonds with four Te atoms, two from top and bottom, respectively). For the out-of-plane structure, each top Te atom pairs with a bottom Te atom to form a Te-Te dimer across the layer⁵, resulting in a puckered layer with a shorter vertical height of 1.69 Å compared with that (2.76 Å) of the monolayer hexagonal PdTe₂¹¹. The atomic-resolution STM image taken after growth reveals one-dimensional zigzag-chains formed by bright dots (Fig. 1e), indicating low-symmetry arrangements of surface atoms. This structure agrees well with the patterns of topmost Te atoms of pentagonal PdTe₂. The measured unit cell of the as-grown structure is square (6.2×6.2 Å), which is slightly different from the previously calculated rectangular lattice for the free-standing monolayer pentagonal PdTe₂ with the unit cell of 6.1×6.4 Å^{8,11}. The reason for this difference can be ascribed to the lattice

confinement from the underlying Pd(100) substrate with a square lattice. We note that unlike the Pd(100) lattice, the as-grown PdTe₂ lattice is not invariant upon 90° rotation even when it has a square unit cell. According to the Pd-Te phase diagram³⁸ and theoretical database of 2D materials^{39,40}, for all known Pd-Te compounds, the pentagonal PdTe₂ we discuss here (β pentagonal phase³) is the only one that has a rectangular-shape unit cell with lattice constants close to 6.2×6.2 Å, consistent with our STM images. While other types of pentagon-based phases have also been predicted for other materials (such as γ phase for PdS₂)^{3,41}, the β pentagonal phase we discuss here is the only one where zigzag chains could be formed by topmost atoms, again consistent with our STM observations thus confirming our structural assignment. We also notice that the as-grown monolayer pentagonal PdTe₂ is stable after air exposure (Supplementary Fig. 3), facilitating its potential applications in ambient conditions.

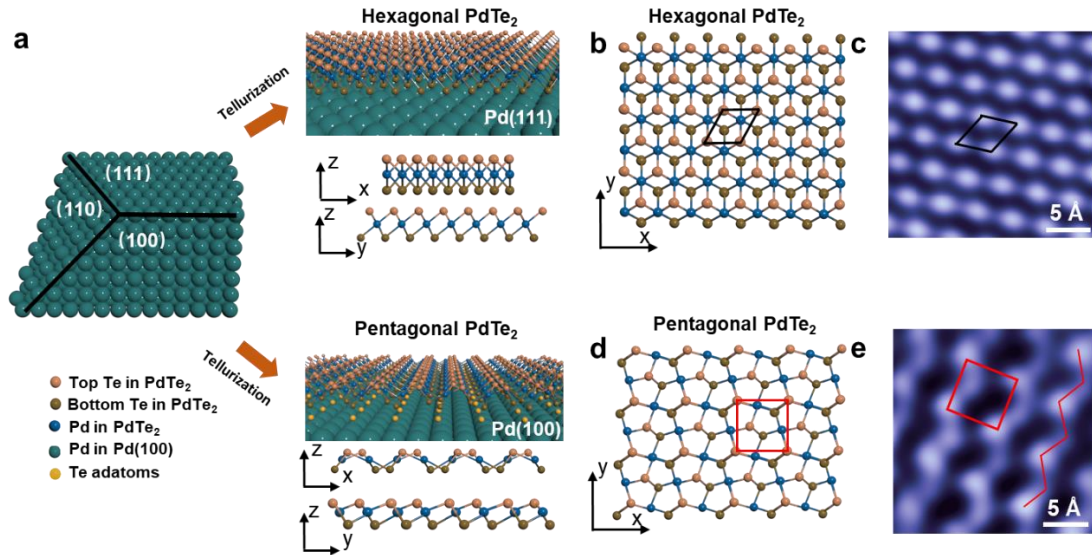


Fig. 1: Synthesis of monolayer hexagonal and pentagonal PdTe₂. **a**, Schematics of epitaxial growth of monolayer hexagonal and pentagonal PdTe₂ by direct tellurization of Pd(111) and Pd(100) surfaces, respectively. This schematic image is for the demonstration of key aspects of the growth method only. Te adatoms in the schematic image of pentagonal PdTe₂ on Pd(100) are discussed in the later text. **b** and **c**, A schematic lattice image (top view) and an atomic-resolved STM image of monolayer hexagonal PdTe₂, respectively. **d** and **e**, A schematic lattice image (top view) and an atomic-resolved STM image of monolayer pentagonal PdTe₂, respectively. Corresponding side views of the lattices shown in **b** and **d** are shown in **a**. Measurement parameters: sample bias voltage $V_b = 0.8$ V, tunneling current magnitude $I_t = 0.7$ nA for

c and $V_b = -0.5$ V, $I_t = 0.5$ nA for **e**. Black rhombuses and red squares represent unit cells of hexagonal and pentagonal PdTe₂, respectively. Red lines in **e** indicate zigzag chains formed by topmost Te atoms.

We carried out synchrotron-based XPS measurements to verify the formation of PdTe₂. We observed two sets of peaks in the Pd 3*d* spectra: one set presents lower binding energies at 335.1 eV and 340.4 eV while the other presents higher binding energies at 336.0 eV and 341.3 eV (Supplementary Fig. 4a). The sets at lower and higher binding energies can be attributed to bulk Pd substrate and pentagonal PdTe₂, respectively. Two sets of Te 4*d* peaks were also observed in the XPS spectra (Supplementary Fig. 4b). The lower binding energies of 40.6 eV and 42.1 eV are ascribed to Te in PdTe₂. The existence of the set of higher binding energies of 41.5 eV and 43.0 eV indicates that there is another type of Te in the system. We attribute it to a Te adatoms layer between the as-grown pentagonal PdTe₂ and the Pd(100) substrate, supported by previous works in similar systems (e.g. TMDC monolayers epitaxially grown on corresponding single crystals)^{42,43} and our DFT calculations (A comparison between the XPS spectra of as-grown pentagonal and hexagonal PdTe₂ demonstrates that Te adatoms are unique in pentagonal PdTe₂/Pd(100), Supplementary Fig. 4c. More discussions about the Te adatoms could be found in Supplementary Fig. 5, Supplementary Table 1 and Supplementary Fig 6). Moreover, we carried out the XPS measurements under both normal and grazing emission angle to determine the relative contribution of PdTe₂, Te adatoms and the Pd(100) substrate (Supplementary Fig. 4a and 4b). The results show the Pd peak area ratio of PdTe₂ to bulk Pd substrate became bigger at grazing emission while the Te peak area ratio of Te adatoms to PdTe₂ became smaller, suggesting that PdTe₂ is on top of Pd(100) and Te adatoms are under PdTe₂. Based on our XPS results, the thickness of the as-grown pentagonal PdTe₂ is estimated^{36,44} to be ~ 1.6 Å, consistent with monolayer pentagonal PdTe₂¹¹. This value is also much smaller than the calculated thickness of bilayer pentagonal PdTe₂ (5.1 Å), indicating the as-grown PdTe₂ is unlikely a bilayer.

In addition, we performed DFT calculations and HREELS measurements to explore the lattice dynamics of monolayer pentagonal PdTe₂. The calculated phonon dispersions of monolayer pentagonal PdTe₂ (Fig. 2a) show dramatically different features from those of monolayer hexagonal PdTe₂ (Supplementary Fig. 7a). In the meantime, HREELS was utilized to experimentally probe the phonon modes. Two components could be

resolved at 23 meV and 26 meV in the energy loss spectrum measured at the Γ point (Fig. 2b), in fair agreement with the calculated optical phonon modes of monolayer pentagonal PdTe₂ and notably different from the measured HREELS spectrum (which shows peaks at 15 meV and 25 meV) in monolayer hexagonal PdTe₂ (Supplementary Fig. 7b). No modes were observed on the Pd(100) substrate in the same energy region (Supplementary Fig. 8), proving the observed energy loss modes are from the as-grown pentagonal PdTe₂.

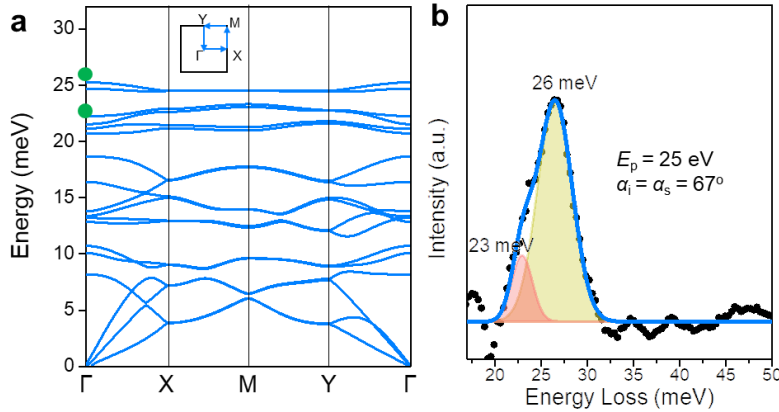


Fig. 2: Phonons of monolayer pentagonal PdTe₂. **a**, Calculated phonon dispersions of monolayer pentagonal PdTe₂ along the Γ -X-M-Y- Γ path of the Brillouin zone as shown in the inset. **b**, An electron energy loss spectrum of as-grown pentagonal PdTe₂ at the Γ point. Dashed black and solid blue curves are the original data curve (after background subtraction) and the fitting curve, respectively. Red and yellow peaks (at 23 meV and 26 meV respectively) are the fitting components and their energies are marked as green dots in **a**. The primary electron beam energy (E_p) is 25 eV. Incident and scattering angles (α_i and α_s , respectively) are 67° .

For a comprehensive understanding of the atomic structures, the as-grown pentagonal PdTe₂ was studied by STM and LEED. After growth, the surface as seen by STM is clean and flat over a large area with sometimes an apparent step height of $\sim 1.9 \text{ \AA}$ (Fig. 3a), consistent with a monoatomic step terrace of Pd(100) and indicating the monolayer PdTe₂ is epitaxially grown on the terrace. Note all the terraces we observed by STM exhibit a vertical height around this value, consistent with the imaged Pd(100) surface being fully covered by monolayer PdTe₂ with no bilayer or multilayer regions found. The magnified STM image shows clear and parallel zigzags chains, implying the well-

ordered structures and high-quality of the as-grown pentagonal PdTe₂ (Fig. 3b). Individual atoms were clearly resolved in the zoomed-in STM image (Fig. 3c), confirming the low-symmetry atomic arrangements of the monolayer pentagonal PdTe₂. The unit cell of pentagonal PdTe₂ is square with dimensions of 6.2×6.2 Å, corresponding to the ($\sqrt{5}\times\sqrt{5}$)R26.6° supercell of the underlying Pd(100) ($\sqrt{5}\times 2.75 = 6.15 \approx 6.2$ Å, where the lattice constant of the surface atoms of Pd(100) is 2.75 Å). Notably, even with a square unit cell, the as-grown pentagonal PdTe₂ exhibits only a two-fold (180°) rotational symmetry rather than four-fold (90°) rotational symmetry of the square lattice of the underlying Pd(100). Occasionally, coexistence of two differently-orientated domains in the as-grown pentagonal PdTe₂ could be observed (Fig. 3d). The angle between the two orientations is ~53° (approximately twice of 26.6°), indicating that each orientation is rotated symmetrically by ~26.6° with respect to the lattice orientation of Pd(100). The *a* axes (the direction along zigzag chains) of the two orientations are along the $[01\bar{2}]$ and $[0\bar{1}2]$ crystallographic directions of the Pd(100) topmost surface respectively, illustrating a good epitaxy (Fig. 3e). Due to the lack of four-fold (90°) rotational symmetry, there could also exist two other possible orientations for the as-grown pentagonal PdTe₂ lattices by rotating the two observed orientations (Fig. 3d) by 90° (the two other possible lattice vectors are along the $[0\bar{2}1]$ and $[02\bar{1}]$ directions as shown in Supplementary Fig. 9, though we have not yet observed PdTe₂ domains along these two directions, possibly due to the small scanning areas of STM). Furthermore, LEED characterizations were carried out to examine the crystallinity and orientation of the as-grown pentagonal PdTe₂ over a millimeter scale. As shown in Fig. 3f, bright and sharp diffraction spots were observed, proving the high crystallinity of the as-grown pentagonal PdTe₂ layer over a large surface area. Two sets of the diffraction patterns with a rotation angle of ~53° between them were clearly identified, which is consistent with the rotation angle between the two domains observed in STM (Fig. 3d). Comparing the LEED patterns of pentagonal PdTe₂ with those of bare Pd(100) (Supplementary Fig. 10), it is further confirmed that each set of the PdTe₂ diffraction patterns is rotated by ~26.6° with respect to the diffraction pattern (lattice orientation) of Pd(100). Note the LEED patterns obtained on the pentagonal PdTe₂ do possess a four-fold (90°) rotational symmetry thus cannot distinguish two orientations that are rotated by 90° from each other (in other words the observed LEED

patterns could be consistent with two to four different orientations coexisting on the surface measured).

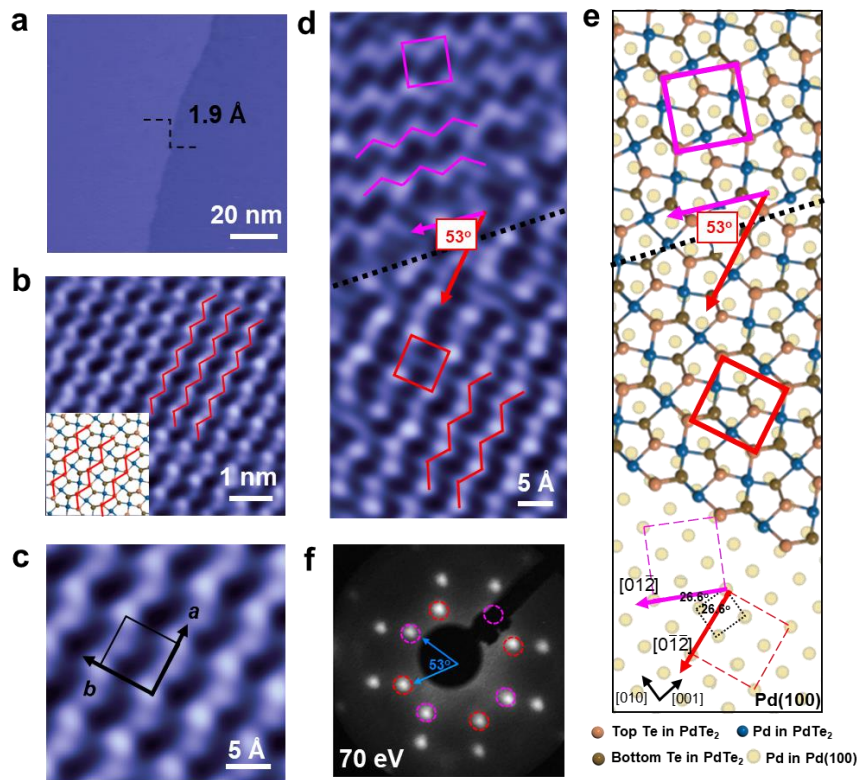


Fig. 3: STM and LEED measurements of the as-grown monolayer pentagonal PdTe₂. **a-c**, Topographic (**a**), magnified (**b**) and atomic-resolution (**c**) STM images of the as-grown pentagonal PdTe₂. $V_b = 1.0$ V, $I_t = 0.5$ nA for **a**. $V_b = -0.5$ V, $I_t = 0.5$ nA for **b** and **c**. Inset of **b**, A schematic image of pentagonal PdTe₂. Red solid lines in **b** represent the zigzag chains formed by Te atoms from the topmost layer. The black square in **c** represents the unit cell of pentagonal PdTe₂. The direction along zigzag chains is a axis. **d**, A STM image of the as-grown pentagonal PdTe₂ showing two crystallographic orientations. $V_b = -0.5$ V, $I_t = 0.5$ nA. The pink and red solid lines represent the zigzag chains formed by Te atoms on the topmost layer. **e**, A schematic image showing a axes of the pentagonal PdTe₂ lattices grown along the $[01\bar{2}]$ and $[0\bar{1}2]$ directions of Pd(100) topmost surface, demonstrating the stacking geometry and epitaxial relationship. The dashed black square represents the unit cell of topmost atoms of Pd(100). Black arrows (lower left) indicate the main crystallographic directions of Pd(100). The red and pink squares (solid and dashed) in **d** and **e** represent the unit cells of pentagonal PdTe₂ in two orientations. Pink and red arrows in **d** and **e** represent two crystallographic orientations of a axes (the direction along zigzag chains) of the as-grown pentagonal

PdTe₂. Each orientation has a rotation angle of 26.6° with respect to the unit cell of the topmost atoms of Pd(100). The black dashed lines in **d** and **e** indicate the grain boundary. Note Te adatoms are invisible in **e** because they are covered by bottom Te atoms of PdTe₂. **f**, LEED patterns of the as-grown pentagonal PdTe₂ measured with a beam energy of 70 eV. Pink and red dashed circles represent the two sets of diffraction patterns. Bright dots without circles are the second order diffraction patterns. LEED patterns from Pd(100) are not observable in this measurement but were measured separately on a bare Pd(100) substrate without changing the crystal orientation (Supplementary Fig. 10).

We carried out further STM measurements and theoretical simulations under various tunneling voltages to explore topographic structures of the pentagonal PdTe₂ and electronic effects. Atomically resolved STM images of pentagonal PdTe₂ exhibit a strong dependence on tunneling biases (Fig. 4), similar to that of bulk PdSe₂⁴⁵. At tunneling biases of 1.0 V and -0.5 V, only features of the zigzag chains formed by topmost Te atoms were resolved (Fig. 4b and 4c). At a large negative tunneling bias of -1.0 V, signals from Pd atoms in the middle layer of PdTe₂ became visible (Fig. 4d). This observed bias-dependence could be explained by the calculated total density of states (DOS) (Fig. 4e), where Pd atoms are found to contribute much more strongly to the DOS at more negative energies (relative to the Fermi level). Therefore, the STM image collected at -1.0 V reveals the combination of topographic and electronic effects, while, at positive and small negative energies, the topographic effect is dominant. The simulated STM images at different biases (Fig. 4f-h) are in agreement with the corresponding experimental STM images, confirming the high quality of the as-grown monolayer pentagonal PdTe₂.

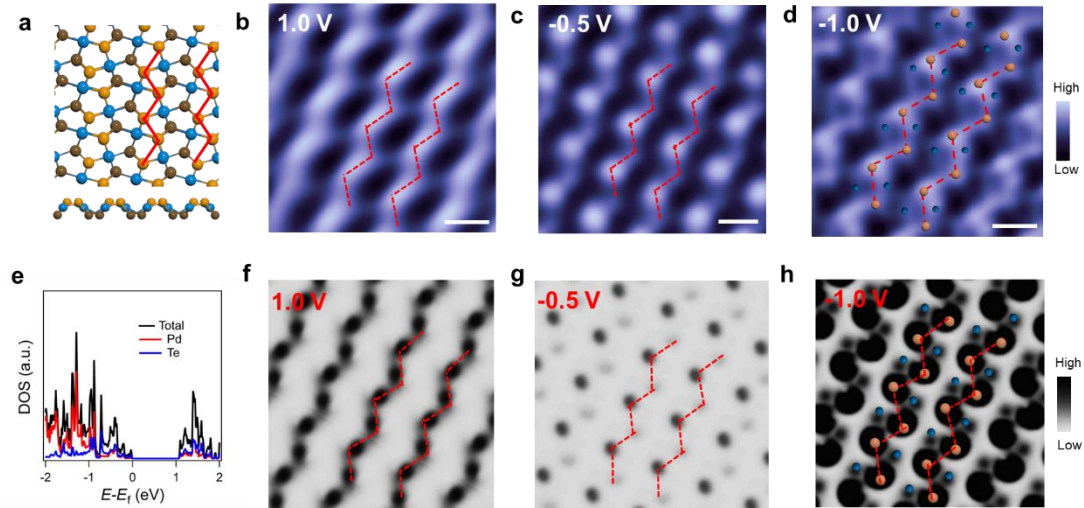


Fig. 4: Experimental and simulated STM images at various bias voltages. **a**, Schematic images of monolayer pentagonal PdTe₂ in top view (upper) and side view (lower). Orange, blue and brown spheres represent top Te, Pd and bottom Te atoms, respectively. **b-d**, Experimental STM images of the as-grown pentagonal PdTe₂ at different biases of 1.0 V, -0.5 V and -1.0 V, respectively. $I_t = 0.5$ nA. **e**, The calculated DOS for monolayer pentagonal PdTe₂. The black curve is the total DOS. The red and blue curves are partial contributions from Pd and Te atoms, respectively. **f-h**, Simulated STM images at different biases of 1.0 V, -0.5 V and -1.0 V, respectively. Red lines (solid and dashed) in all images indicate the zigzag chains formed by Te atoms from the topmost layer. Orange and blue dots in **d** and **h** indicate the Te atoms on the topmost layer and Pd atoms on the middle layer in the PdTe₂, respectively. Note the experimental and simulated STM images have opposite color scales.

To further understand the electronic structures, we performed DFT calculations for the electron band structures of monolayer pentagonal PdTe₂. The valence band maximum (VBM) of monolayer pentagonal PdTe₂ is along the Γ -X path (defined as along the zigzag chain direction in our calculation) while the conduction band minimum (CBM) is along the Γ -Y path (perpendicular to the zigzag chain direction), leading to an indirect bandgap of 1.05 eV (Fig. 5a and Supplementary Fig. 11), which is dramatically different from the narrow indirect bandgap of monolayer hexagonal PdTe₂ of 0.33 eV (Supplementary Fig. 12). Valence band structures along three high-symmetry directions, Y- Γ -Y, X- Γ -X and M- Γ -M, were plotted and valence bands dispersed in a “M shape” were observed in all the three directions near the Fermi level

(Supplementary Fig. 13). The calculated value of the bandgap and main features of the band structures are comparable with previous calculated results^{8,10,11}. To confirm the semiconducting nature and probe the bandgap, we performed STS measurements. The STS curve of the as-grown monolayer pentagonal PdTe₂ shows a suppressed conductance region with two onsets of ~ -0.6 V and ~ 0.6 V, leading to an estimated bandgap of ~ 1.2 eV (Fig. 5b). This is in reasonable agreement with the calculated 1.05 eV bandgap of monolayer pentagonal PdTe₂ (noting DFT calculations are known to underestimate the bandgap^{46,47} and were performed on free standing pentagonal PdTe₂). Meanwhile the ~ 1.2 eV bandgap is much bigger than the calculated 0.39 eV bandgap for bilayer and zero bandgap for trilayer pentagonal PdTe₂ (Supplementary Fig. 14), further suggesting the as-grown PdTe₂ is monolayer. The small nonzero conductance within the bandgap in the STS curve could be attributed to the tunneling to the Pd substrate, as commonly observed in STS curves of monolayer 2D semiconducting materials on metallic substrates^{48,49}. We also conducted ARPES measurements to further probe the band structures of monolayer pentagonal PdTe₂ (note only valence bands were measured since the conduction bands lie above the Fermi level). ARPES results of the as-grown PdTe₂ and clean Pd(100) substrate extracted along a Γ - Γ -Y direction (inset of Fig. 5c) are shown in Fig. 5c and 5d, respectively. Since domains of four orientations of pentagonal PdTe₂ could be present simultaneously on the surface, band dispersion cutting from the Γ -Y direction of one orientation domain could be superimposed with contributions from domains of other possible orientations, approximately in the Γ -M and Γ -X directions (Supplementary Fig. 15). Given the similarity of the dispersion in the Γ -Y, Γ -M and Γ -X directions (Supplementary Fig. 13), this would merely result in a broadened band of “M shape” valence band. The observed “M-shaped” dispersing band located at ~ -0.65 eV at the Γ point is thus consistent with the calculated valence band structures. This “M shaped” band was also observed along the Γ -X direction (Supplementary Fig. 16). In addition to the broadening by the simultaneous presence of differently-orientated domains, the PdTe₂ bands are likely to experience additional broadening and change of dispersion due to the interaction with the substrate. On the other hand, the “M shaped” band clearly retains a two-dimensional character as it does not disperse with different photon energies (Fig. 5e), suggesting the 2D nature of the monolayer pentagonal PdTe₂.

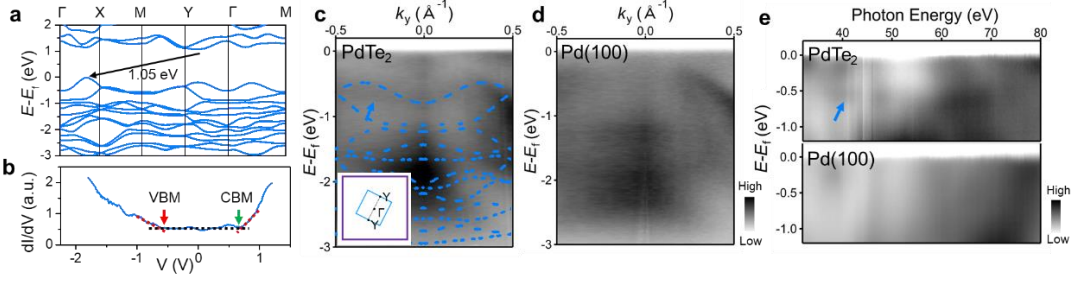


Fig. 5: Band structures of monolayer pentagonal PdTe₂. **a**, Calculated band structures of monolayer pentagonal PdTe₂ with spin-orbital coupling (SOC). **b**, A STS spectrum of monolayer pentagonal PdTe₂ on Pd(100). $V_b = -100$ mV, $I_t = 50$ pA. The ~ 1.2 eV bandgap is obtained by measuring the intersections of sharp rises (red dashed lines) and the baseline value of the conductance (black dashed line). Red and green arrows indicate the intersections, corresponding to energies near VBM and CBM, respectively. **c**, Overall ARPES results of monolayer pentagonal PdTe₂ extracted along Y- Γ -Y direction (defined for one domain orientation relative to the substrate Brillouin zone as indicated in the inset). The blue arrow points to the “M shape” valence band. The calculated band structures along the Y- Γ -Y direction are superimposed with blue dashed lines. The ARPES result without superimposed calculated band structures is shown in the Supplementary Fig. 17. Inset: Brillouin zones of one pentagonal PdTe₂ domain (blue square) and underlying Pd(100) substrate (larger purple square). **d**, ARPES result of clean Pd(100) substrate extracted along the same direction with that in **c**. **e**, Photon energy-dependent spectra at the Γ points for pentagonal PdTe₂ (upper panel) and clean Pd(100) (lower panel). The blue arrow points to the non-dispersion pentagonal PdTe₂-related band.

In conclusion, we demonstrated the tellurization-based direct synthesis of metastable monolayer pentagonal PdTe₂ driven by symmetry epitaxy and provided comprehensive characterizations on this pentagonal 2D material. As confirmed by STM and LEED, the as-grown pentagonal PdTe₂ exhibited one-dimensional zigzag atomic chains, with the unit cell matching the $(\sqrt{5} \times \sqrt{5})R26.6^\circ$ supercell of the underlying Pd(100) substrate. XPS verified the formation of PdTe₂ and suggested its monolayer thickness. Experimentally measured HREELS spectrum probed its lattice vibrations and was consistent with the calculated phonon modes of monolayer pentagonal PdTe₂. The

experimental STM images of monolayer pentagonal PdTe₂ at various bias voltages showed strong bias-dependence, which is also clearly revealed in the simulated STM images. Calculated band structures demonstrated monolayer pentagonal PdTe₂ is a semiconductor with an indirect bandgap of 1.05 eV, which agrees with the STS-measured bandgap. The valence band structures were further measured by ARPES, with features consistent with the calculations. The symmetry-driven epitaxial growth provides a viable way for the synthesis of pentagon-based 2D materials, even for metastable phases. Our method will add this unique group of materials to the 2D materials family, so far dominated by hexagon-based ones, and expand it to include a large number of low-symmetry members. This will also bring unprecedented opportunities for 2D materials in applications such as functional electronics based on the in-plane anisotropy, optoelectronics originated from the non-linear light-matter interaction and thermoelectric devices benefited from the low thermal conductivity.

Acknowledgements

L.L., D.Z., and Y.C. acknowledge partial financial support by the U.S. Department of Energy (Office of Basic Energy Sciences) under Award No. DE-SC0019215 (for synthesis) and Multidisciplinary University Research Initiatives (MURI) Program under Award No. FA9550-20-1-0322 (for characterizations). Y.J. and Y.L. acknowledge support by Natural Science Foundation of Jiangsu Province (BK20200873, BZ2020011) and National Natural Science Foundation of China (Grants No. 22173067). M.B., J.M. and P.H. acknowledge support by VILLUM FONDEN via the Centre of Excellence for Dirac Materials (Grant No. 11744). L.L., R.B., and Y.C. also acknowledge support by VILLUM FONDEN via the Villum Investigator program (Grant No. 25931). Part of the STM measurements (at low temperature) were performed in the Center for Nanophase Materials Sciences (CNMS), which is a US Department of Energy, Office of Science User Facility at Oak Ridge National Laboratory. We express our gratitude to the Center for Nanoscale Materials of Argonne National Laboratory and in particular to Dr. Nathan P Guisinger for the help with the STM tip preparation. We also acknowledge helpful discussions with Espen Drath Bøjesen, Cliff Bugge, Rosa E. Diaz, Yuichi Ikuhara, Lasse Hyldgaard Klausen, Toru Koyama, Akichika Kumatani, Krishna Kanth Neelisetty and the team at Thermo Fisher Scientific, Mitsuhiro Saito, Jim Smith, and Ouyang Yi.

Author Contributions

L.L. and D.Z. designed the experiments. L.L. and D.Z. performed the experiments and data analysis. Y.J. and Y.L. performed the DFT calculations. M.B., R.B., J.M. and P. H. performed the ARPES measurements and data analysis. S.H and A.L performed the STS measurements and data analysis. Z.L. worked on the synchrotron-based XPS measurements and data analysis. Y.C. coordinated the collaboration and advised the project. L.L. wrote the paper with input from all other co-authors. All authors discussed the results and gave approval of the final version.

Competing interests

The authors declare no competing interests.

Methods

Growth of monolayer pentagonal PdTe₂. Epitaxial growth was conducted in an UHV preparation chamber with a base pressure of 1×10^{-9} mbar. Pd(100) single crystal was used after repeated cycles of Ar⁺ sputtering (1kV, 10 mA for 10 min at a Ar background pressure of $\sim 1.0 \times 10^{-6}$ mbar) and annealing (~ 700 °C for 20 min) until clear diffraction patterns were observed by LEED. Tellurium (99.999%, Sigma-Aldrich) was thermally evaporated using a home-built evaporator equipped in the preparation chamber. The substrate was kept at room temperature (RT) during deposition. Te source was kept at ~ 295 °C for 20 min for evaporation. After deposition, annealing was conducted at 500 °C for 20 min for the PdTe₂ growth presented in the main text.

Characterizations of as-grown PdTe₂. STM, LEED, XPS and HREELS measurements were done at RT (except otherwise noted) in an analysis chamber connected to the preparation chamber with a base pressure of 10^{-11} mbar. STM images (Omicron ambient temperature UHV STM) were collected using electrochemically etched W tips at a constant current (topographic) mode (with tips grounded) and were processed using the software WSxM. LEED measurements were conducted with a four-grid optics (Omicron LEED). Lab-based XPS was acquired using a non-monochromatic Mg K α X-ray radiation ($h\nu=1253.6$ eV) at 150 W. High resolution spectra were recorded at a constant pass energy of 20 eV using the electron energy analyzer-Omicron EAC 125 and the analyzer controller-Omicron EAC 2000. XPS results were analyzed using CasaXPS. The Finite Lorentzian (LF) function and Shirley background function were used for the line shape and background fittings (unless

elsewhere noted), respectively. HREELS was performed with ELS5000 from LK technologies. The primary electron beam energy used in this work was 25 eV. The incident and scattering angles were 67° . STS measurements were carried out at 100 K in a separate Omicron variable temperature (VT) STM. Synchrotron-based XPS was collected at the ASTRID2 synchrotron (MatLine) facility at Aarhus University. The MatLine is equipped with an SX-700 monochromator and a SPECS PHOIBOS 150 electron energy analyzer⁵⁰. The analyzer was operated at a pass energy of 20 eV and a curved analyzer slit of 0.8 mm. The beamline monochromator exit slit was set to a width of 30 μm . Photon energies of 410 eV and 80 eV were used for acquiring the Pd 3d and Te 4d spectra, respectively. ARPES spectra were acquired at the SGM3 beamline⁵¹ at ASTRID2⁵², using different photon energies in the range from 20 eV to 130 eV. The data shown in the main text have been acquired using linearly polarized light of 70 eV at 45 K with a combined energy and angle resolution better than 40 meV and 0.2° . The beam spot size on the sample is about $190 \times 90 \mu\text{m}$ and linearly polarized. The monolayer pentagonal PdTe₂ and clean Pd(100) in the synchrotron facility were prepared *in situ* with analogous methods from those presented earlier, with quality and crystallinity cross-checked with a home-built room temperature Aarhus XPS, STM and LEED to confirm the consistency. Fermi surface mapping obtained by ARPES helped to determine the high symmetry crystal axes of PdTe₂ relative to the Pd(100) substrate.

DFT calculations. All calculations were conducted in the Vienna *ab-initio* Software Package version 5.4.1 in the framework of density functional theory with the basis sets of the projector augmented wave⁵³⁻⁵⁶. We adopted the revised Perdew-Burke-Ernzerhof (PBE) functional under Pade approximation⁵⁷ for geometry optimization in a primitive cell (detailed information is provided in the public repository <https://github.com/Austin6035/DFT-characterization-of-PdTe2-on-Pd>). We set up a model with Te adatoms on the Pd substrate surface (Supplementary Fig. 5b), constituting a buffer layer with Te atoms staying on the hollow sites of Pd(100), between Pd(100) and PdTe₂. This model was built because our XPS results (Supplementary Fig. 4b) and a few previous studies suggested the existence of a buffer layer in similar systems (TMDC monolayers epitaxially grow on corresponding single crystals^{42,43}). After structural optimization with the model, all calculated results were based on free-standing monolayer pentagonal PdTe₂ with the optimized structure. Band structures were calculated with the PBE functional. The kinetic cut-off energy was set to 450 eV and the thresholds of total energy and Feynman-Hellman force during

structural optimizations were 10^{-4} eV and -0.01 eV/Å, respectively. The Gamma-centered Monkhorst-Pack grids of $4\times 4\times 1$ were sampled in the Brillouin zones. A vacuum space of 15 Å was added along the z direction to avoid the periodic imaging influence. Phonon dispersions of monolayer pentagonal and hexagonal PdTe₂ were calculated with the local density approximation (LDA) functional.

References

1. Zhang, S. *et al.* Penta-graphene: a new carbon allotrope. *Proc. Natl. Acad. Sci.* **112**, 2372-2377 (2015).
2. Wang, Y., Li, Y. & Chen, Z. Not your familiar two-dimensional transition metal disulfide: structural and electronic properties of the PdS₂ monolayer. *J Mater. Chem. C* **3**, 9603-9608 (2015).
3. Shen, Y. & Wang, Q. Pentagon-based 2D materials: classification, properties and applications. *Phys. Rep.* **964**, 1-42 (2022).
4. Liang, Q. J., Chen, Z. L., Zhang, Q. & Wee, A. T. S. Pentagonal 2D transition metal dichalcogenides: PdSe₂ and beyond. *Adv. Funct. Mater.* **32**, 2203555 (2022).
5. Kempt, R., Kuc, A. & Heine, T. Two-dimensional noble-metal chalcogenides and phosphochalcogenides. *Angew. Chem. Int. Ed.* **59**, 9242-9254 (2020).
6. Gu, Y. *et al.* Two-dimensional palladium diselenide with strong in-plane optical anisotropy and high mobility grown by chemical vapor deposition. *Adv. Mater.* **32**, e1906238 (2020).
7. Jiang, S. *et al.* Anisotropic growth and scanning tunneling microscopy identification of ultrathin even-layered PdSe₂ ribbons. *Small* **15**, e1902789 (2019).
8. Lan, Y.-S., Chen, X.-R., Hu, C.-E., Cheng, Y. & Chen, Q.-F. Penta-PdX₂ (X = S, Se, Te) monolayers: promising anisotropic thermoelectric materials. *J. Mater. Chem. A* **7**, 11134-11142 (2019).
9. Tao, W. L., Zhao, Y. Q., Zeng, Z. Y., Chen, X. R. & Geng, H. Y. Anisotropic thermoelectric materials: pentagonal PtM₂ (M = S, Se, Te). *ACS Appl. Mater. Interfaces* **13**, 8700-8709 (2021).
10. Marfoua, B. & Hong, J. High thermoelectric performance in hexagonal 2D PdTe₂ monolayer at room temperature. *ACS Appl. Mater. Interfaces* **11**, 38819-38827 (2019).
11. Xiong, W., Huang, K. & Yuan, S. The mechanical, electronic and optical properties of two-dimensional transition metal chalcogenides MX₂ and M₂X₃ (M = Ni, Pd; X = S, Se, Te) with hexagonal and orthorhombic structures. *J. Mater. Chem. C* **7**, 13518-13525 (2019).
12. Ma, Y., Kou, L., Li, X., Dai, Y. & Heine, T. Room temperature quantum spin Hall states in two-dimensional crystals composed of pentagonal rings and their quantum wells. *NPG Asia Mater.* **8**, e264 (2016).
13. Li, X. Y., Meng, S. & Sun, J. T. Emergence of d-orbital magnetic Dirac fermions in a MoS₂ monolayer with squared pentagon structure. *Phys. Rev. B* **101**, 144409 (2020).
14. Li, X. *et al.* Monolayer puckered pentagonal VTe₂: An emergent two-dimensional ferromagnetic semiconductor with multiferroic coupling. *Nano Res.* **15**, 1486-1491 (2021).
15. Oyedele, A. D. *et al.* PdSe₂: pentagonal two-dimensional layers with high air stability for electronics. *J. Am. Chem. Soc.* **139**, 14090-14097 (2017).
16. Li, P. *et al.* Penta-PdPSe: A new 2D pentagonal material with highly in-plane optical, electronic, and optoelectronic anisotropy. *Adv. Mater.* **33**, e2102541 (2021).
17. Chow, W. L. *et al.* High mobility 2D palladium diselenide field-effect transistors with tunable ambipolar characteristics. *Adv. Mater.* **29**, 1602969 (2017).
18. Duan, R. *et al.* 2D Cairo pentagonal PdPS: air-stable anisotropic ternary semiconductor with high optoelectronic performance. *Adv. Funct. Mater.* **32**, 2113255 (2022).

19. Folmer, J. C. W., Turner, J. A. & Parkinson, B. A. Amelioration of the photoresponse of PdPS photoanodes by ferrocyanide electrolytes. *Inorg. Chem.* **24**, 4028-4030 (1985).
20. Folmer, J. C. W., Turner, J. A. & Parkinson, B. A. Photoelectrochemical characterization of several semiconducting compounds of palladium with sulfur and/or phosphorus. *J. Solid State Chem.* **68**, 28-37 (1987).
21. Yu, J. *et al.* Giant nonlinear optical activity in two-dimensional palladium diselenide. *Nat. Commun.* **12**, 1083 (2021).
22. Jia, L., Wu, J., Yang, T., Jia, B. & Moss, D. J. Large third-order optical Kerr nonlinearity in nanometer-thick PdSe₂ 2D dichalcogenide films: implications for nonlinear photonic devices. *ACS Appl. Nano Mater.* **3**, 6876-6883 (2020).
23. Oyedele, A. D. *et al.* Defect-mediated phase transformation in anisotropic two-dimensional PdSe₂ crystals for seamless electrical contacts. *J. Am. Chem. Soc.* **141**, 8928-8936 (2019).
24. Lin, J. *et al.* Novel Pd₂Se₃: two-dimensional phase driven by interlayer fusion in layered PdSe₂. *Phys. Rev. Lett.* **119**, 016101 (2017).
25. Guo, Y. G., Zhou, J., Xie, H. H., Chen, Y. Y. & Wang, Q. Screening transition metal-based polar pentagonal monolayers with large piezoelectricity and shift current. *Npj Comput. Mater.* **8**, 40 (2022).
26. Fang, Y. *et al.* Structure re-determination and superconductivity observation of bulk 1T MoS₂. *Angew. Chem. Int. Ed.* **57**, 1232-1235 (2018).
27. Liu, L. *et al.* Phase-selective synthesis of 1T' MoS₂ monolayers and heterophase bilayers. *Nat. Mater.* **17**, 1108-1114 (2018).
28. Zhang, Q. *et al.* Simultaneous synthesis and integration of two-dimensional electronic components. *Nat. Electron.* **2**, 164-170 (2019).
29. D'Olimpio, G. *et al.* PdTe₂ Transition-metal dichalcogenide: chemical reactivity, thermal stability, and device implementation. *Adv. Funct. Mater.* **30**, 1906556 (2019).
30. Zheng, J. *et al.* Chemical synthesis and integration of highly conductive PdTe₂ with low-dimensional semiconductors for p-type transistors with low contact barriers. *Adv. Mater.* **33**, e2101150 (2021).
31. Liu, C. *et al.* Two-dimensional superconductivity and topological states in PdTe₂ thin films. *Phys. Rev. Mater.* **2**, 094001 (2018).
32. Liu, W. *et al.* New Verbeekite-type polymorphic phase and rich phase diagram in the PdSe_{2-x}Te_x system. *Phys. Rev. B* **104**, 024507 (2021).
33. Chen, T. A. *et al.* Wafer-scale single-crystal hexagonal boron nitride monolayers on Cu (111). *Nature* **579**, 219-223 (2020).
34. Li, T. *et al.* Epitaxial growth of wafer-scale molybdenum disulfide semiconductor single crystals on sapphire. *Nat. Nanotechnol.* **16**, 1201-1207 (2021).
35. Dong, J., Zhang, L., Dai, X. & Ding, F. The epitaxy of 2D materials growth. *Nat. Commun.* **11**, 5862 (2020).
36. Liu, L., Zemlyanov, D. & Chen, Y. P. Epitaxial growth of monolayer PdTe₂ and patterned PtTe₂ by direct tellurization of Pd and Pt surfaces. *2D Mater.* **8**, 045033 (2021).
37. Li, E. *et al.* High quality PdTe₂ thin films grown by molecular beam epitaxy. *Chin. Phys. B* **27**, 5 (2018).
38. Okamoto, H. The Pd-Te system (palladium-tellurium). *JPE* **13**, 73-78 (1992).
39. Gjerding, M. N. *et al.* Recent progress of the computational 2D materials database (C2DB). *2D Mater.* **8**, 044002 (2021).
40. Haastrup, S. *et al.* The computational 2D materials database: high-throughput modeling and discovery of atomically thin crystals. *2D Mater.* **5**, 042002 (2018).
41. Zhang, W., Cui, Y., Zhu, C., Huang, B. & Yan, S. Flexible ferroelasticity in monolayer PdS₂: a DFT study. *Phys. Chem. Chem. Phys.* **23**, 10551-10559 (2021).
42. Bosnar, M., Caciuc, V., Atodiresei, N., Lončarić, I. & Blügel, S. Se intercalation between PtSe₂ and the Pt surface during synthesis of PtSe₂ by direct selenization of Pt(111). *Phys. Rev. B* **102**, 115427 (2020).
43. Perea Acosta, J., Barral, M. A. & Maria Llois, A. Monolayer of PtSe₂ on Pt(111): is it

- metallic or insulating? *J. Phys. Condens. Matter.* **32**, 235002 (2020).
44. Zemlyanov, D. Y. *et al.* Versatile technique for assessing thickness of 2D layered materials by XPS. *Nanotechnology* **29**, 115705 (2018).
 45. Fu, M. *et al.* Defects in highly anisotropic transition-metal dichalcogenide PdSe₂. *J. Phys. Chem. Lett.* **11**, 740-746 (2020).
 46. Perdew, J. P. & Levy, M. Physical content of the exact Kohn-Sham orbital energies: bandgaps and derivative discontinuities. *Phys. Rev. Lett.* **51**, 1884-1887 (1983).
 47. Verma, P. & Truhlar, D. G. HLE16: a local Kohn-Sham gradient approximation with good performance for semiconductor band gaps and molecular excitation energies. *J. Phys. Chem. Lett.* **8**, 380-387 (2017).
 48. Sorensen, S. G., Fuchtbauer, H. G., Tuxen, A. K., Walton, A. S. & Lauritsen, J. V. Structure and electronic properties of in situ synthesized single-layer MoS₂ on a gold surface. *ACS Nano* **8**, 6788-6796 (2014).
 49. Tumino, F., Casari, C. S., Passoni, M., Russo, V. & Li Bassi, A. Pulsed laser deposition of single-layer MoS₂ on Au(111): from nanosized crystals to large-area films. *Nanoscale Adv.* **1**, 643-655 (2019).
 50. ISA. Centre for Storage Ring Facilities, Aarhus., <<http://www.isa.au.dk/>> (2020).
 51. Hoffmann, S., Søndergaard, C., Schultz, C., Li, Z. & Hofmann, P. An undulator-based spherical grating monochromator beamline for angle-resolved photoemission spectroscopy. *Nucl. Instrum. Methods Phys. Res. A* **523**, 441-453 (2004).
 52. Bianchi, M., Hofmann, P., Hoffmann, S.V. *et al.* Status and strategy at ISA, centre for storage ring facilities, Aarhus University, Denmark. *Eur. Phys. J. Plus* **138**, 132 (2023).
 53. Hohenberg, P. & Kohn, W. Inhomogeneous electron gas. *Phys. Rev.* **136**, B864-B871 (1964).
 54. Blöchl, P. E. Projector augmented-wave method. *Phys. Rev. B* **50**, 17953-17979 (1994).
 55. Kresse, G. & Joubert, D. From ultrasoft pseudopotentials to the projector augmented-wave method. *Phys. Rev. B* **59**, 1758-1775 (1999).
 56. Kresse, G. & Furthmüller, J. Efficient iterative schemes for *ab initio* total-energy calculations using a plane-wave basis set. *Phys. Rev. B* **54**, 11169-11186 (1996).
 57. Hammer, B., Hansen, L. B. & Nørskov, J. K. Improved adsorption energetics within density-functional theory using revised Perdew-Burke-Ernzerhof functionals. *Phys. Rev. B* **59**, 7413-7421 (1999).